Conductivity Relaxation in Zirconia Nanoparticles Dispersed in Conducting Polymer

Ashis Dey, S. K. De

Department of Materials Science, Indian Association for the Cultivation of Science, Jadavpur, Kolkata 700 032, India

Received 9 September 2006; accepted 30 November 2006
DOI 10.1002/app.26218
Published online 26 April 2007 in Wiley InterScience (www.interscience.wiley.com).

ABSTRACT: Zirconia-polyaniline (ZrO_2-PANI) nanocomposites have been synthesized using the colloidal stability of ZrO_2 sol. Complex impedance and dielectric permittivity of ZrO_2-PANI nanocomposites have been investigated as a function of frequency and temperature for different compositions. Grain conductivity is about two orders of magnitude higher than the grain boundary conductivity. A very large dielectric permittivity of about 2500 at room temperature has been observed for the composite with highest content of ZrO_2. The high dielectric permittivity is mainly dominated by interfacial polarization because of Maxwell-Wagner relaxation effect. The electric modulus spectra reveal two types of conductivity relaxation. © 2007 Wiley Periodicals, Inc. J Appl Polym Sci 105: 2225–2235, 2007

Key words: dielectric properties; charge transport; conducting polymers; nanocomposites

INTRODUCTION

Zirconia (ZrO_2), one of the important wide band gap transition metal oxides, has been extensively studied because of potential applications[1] in sensors, fuel cells,[2] catalyst,[3] and gate dielectrics.[4,5] ZrO_2 exists in different crystalline phases such as monoclinic, tetragonal, and cubic at elevated temperatures.[6] The high temperature phases can be stabilized by doping with lower valence cations at Zr sites.[7] Oxygen vacancies are created due to the presence of the aliovalent cations within Zr lattice. Doped and reduced ZrO_2 exhibit mixed ionic and electronic conduction depending on temperature and oxygen partial pressure. The electrical properties of polycrystalline materials are mainly determined by the microstructure. The powdered ceramics exhibit distinct grain and grain boundary in their microstructures. Discontinuity in lattice periodicity, different thermodynamics and distribution of oxygen vacancy, and formation of impurity phase of nanoparticle significantly alters the grain boundary properties.[8] The properties of nanocrystalline ZrO_2 are changed because of the presence of high density of interfaces. Grain size and intergrain distances are the important parameters to control the electrical conduction. Nanoscale grain size enhances the conductivity of yttria stabilized ZrO_2 by one or two orders of magnitude than that of microcrystalline sample.[9] Electrical conductivity of sol-gel derived rare earth doped nanocrystalline ZrO_2 thin film is about four times higher than the bulk value.[10] The conductivity of yttria stabilized ZrO_2 films of nanometer thickness is lower by a factor of four compared to the bulk conductivity.[11] Electrical properties of nanocrystalline ZrO_2 critically depend on the techniques of synthesis.

The electrical and dielectric studies of an isolated nanoparticles are very difficult. In this respect, the dispersion of nanosized particles within a suitable matrix is essential to investigate the physical properties as well as to design novel materials. The composites of conducting polymers containing inorganic nanoparticles have attracted much attention in the recent past. The combined effects of organic and inorganic compounds yield a completely different class of materials.[12,13] Polyaniline (PANI) is the most attractive conducting polymer because of its high electrical conductivity and thermal stability. Synthesis of ZrO_2 nanoparticle in PANI[14] and polypyrrole[15,16] and some preliminary characterizations have been reported. In this article, we present the electrical and dielectric properties of PANI-ZrO_2 nanocomposites at low temperature and high frequency employing impedance spectroscopy.

EXPERIMENTAL DETAILS

Aniline and ammonium peroxydisulphate (APS) were purchased from E. Merck (India). Aniline was distilled twice under reduced pressure and stored below 4°C in nitrogen atmosphere. APS was used as received.

Correspondence to: S. K. De (msskd@mahendra.iacs.res.in).
Contract grant sponsor: Department of Atomic Energy, Government of India; contract grant number: 2001/37/4/BRNS.

Journal of Applied Polymer Science, Vol. 105, 2225–2235 (2007)

TABLE I
Weight Percentage of Aniline (x), Room Temperature Dielectric Constant (ε_1) at 40 kHz, Grain Boundary Conductivity (σ_{gb}), Grain Conductivity (σ_g) at Room Temperature, Grain Boundary Activation Energy (E_{gb}), Grain Activation Energy (E_g) and Activation Energy E_M(A) from Peak A, and E_M(B) from Peak B of Conductivity Relaxation

Sample	x	ε_1 (40 kHz)	σ_{gb} (10^{-5} S/cm)	σ_g (10^{-3} S/cm)	E_{gb} (meV)	E_g (meV)	E_M (A) (meV)	E_M (B) (meV)
C1	67.1	2503	0.09	0.03	144	141	121	
C2	80.3	2191	2.62	0.79	73	71	74	
C3	85.9	1563	3.68	2.06	59	57	52	71
C4	89.1	1374	33.74	46.20	72	47	71	
C5	91.1	975	55.03	104.0	63	43	48	
C6	100.0	362						

ZrO_2 nanoparticles have been prepared by a two reverse emulsion technique.[17–19] A typical synthesis involved the following steps.

Zirconium oxychloride solution (0.05*M*) was prepared by dissolving the required amount of Zirconium oxychloride octahydrate, $ZrOCl_2$, $8H_2O$ (G.R., Merck, India) in deionized water.

Support solvents were prepared at ambient temperature by mixing cyclohexane of dielectric constant 2.042 at and 2 vol % of the emulsifier (surfactant) with respect to the cyclohexane under agitation. The sorbitan monooeleate (Span 80, Fluka Chemica AG, Switzerland) having a hydrophilic-lipophilic balance (HLB) value of 4.3 was used as the emulsifier in the present study.

Reverse emulsion of zirconium oxychloride solution (emulsion A) was prepared by adding a measured volume of the salt solution to the support solvent in a closed glass container under a mechanical agitation. The volume ratio of the salt solution : support solvent was 1 : 4 in the experiments. The emulsion B was prepared at ambient temperature by adding a measured volume of the ammonia solution to the support solvent in a closed glass container under mechanical agitation. The volume ratio of the ammonia solution: support solvent was 1 : 4 in the experiment.

Both the containers i.e. the emulsion A and emulsion B were kept separately in an oil bath preheated to 90°C (reaction temperature) and kept at that temperature for 10 min under magnetic stirring to attain the reaction temperature. After attaining the temperature of 90°C, the emulsion B was rapidly added to the emulsion A under stirring to obtain a single reverse emulsion (w/o) followed by simultaneous precipitation of the precursor powders. Ageing at 90°C was continued for 10 min after which the container was removed from the bath and cooled down under water tap. The synthesized particles were obtained from the single reverse emulsions by adding a known volume of acetone. Immediate separation of the particles occurred. The particles were collected by centrifugation. To remove the traces of adhered impurities, the above procedure was repeated twice, each time collecting the powders centrifugally. The washed particles were dried at 100°C in an air oven.

ZrO_2 sol was prepared by dissolving a known amount (1 g) of finely divided powder in double distilled water. The sol was dialyzed until free from all unwanted ions. The nanocomposites of PANI-ZrO_2 were prepared as follows. Fifty milliliter of ZrO_2 colloid was taken at each time and the volume was reduced to about 20 mL on evaporation at −35°C using a lyophilizer. Different volume of aniline (0.1–0.5 mL) was injected to the colloid under ultrasonic action to reduce the agglomeration of ZrO_2 nanoparticles. About 1.5*M* of acidic aqueous solution of APS (precooled) using varying amount of concentrated HCl and keeping 1 : 1.25 monomers: APS mole ratio was then added dropwise under sonication. The polymerization was allowed to proceed for 24 h maintaining the temperature at 0–5°C. The composite came out as bright green residue. The solution was then washed several times with 1.5*M* HCl and deionized water under ultra centrifugation followed by drying in vacuum oven at 60°C for 24 h to obtain fine green powder. Five different compositions (C1–C5) with varying concentration of aniline and pure PANI (C6) as shown in Table I were investigated in details.

CHARACTERIZATION

Particle size and morphology of the bare nanoparticles and the nanocomposites were determined from scanning and transmission electron microscopic studies. X-ray Diffraction (XRD) pattern of the nanocomposites were performed using a Philips Diffractometer (PW 1710) using Cu K_α radiation. UV-Vis spectra of the stable dispersion of nanocomposites and bare nanoparticles were recorded using UV-2401PC (Shimadzu, Japan) spectrometer.

The complex dielectric function, $\varepsilon^* = \varepsilon_1 + i\varepsilon_2$ was obtained from the measurements of capacitance (C) and dissipation factor (D) by autobalance bridge 4192A Agilent Impedance Analyser up to the frequency of 1.6 MHz with an applied ac voltage of 1 V. Agilent test lead 16048A with coaxial cable at room temperature and two-electrode configuration in the cryostat for low temperatures were used. The temperature was varied from 303 to 123 K in a liquid nitro-

gen cryostat using Eurotherm temperature controller, Model No. 2404. The samples for measurements were prepared by uniaxial pressure in a stainless steel die. The samples were disk shaped of 8–10 mm diameter and 0.7–1.0 mm thickness. The electrical contacts on both sides of the pelletized samples were made by silver paint. All the measurements were carried out by a computer based on general purpose interface board (GPIB). The real part of dielectric constant (ε_1) was evaluated by the relation $C = \varepsilon_0\varepsilon_1 S/t$, ε_0 is the permittivity of vacuum, S is the area, and t is the thickness of the sample. The imaginary component was calculated from the dissipation factor, $\varepsilon_2 = D\varepsilon_1$.

RESULTS

Figure 1(a,b) show the characteristic peaks of XRD of bare ZrO_2 nanoparticles and the nanocomposite sample (C1) with highest content of ZrO_2. The main peaks at $2\theta = 30.3^\circ$ (111), 35.3° (200), 50.5° (220), 60.3° (311), 63.0° (222), and 74.6° (400), which are characteristics of tetragonal ZrO_2 are also present in the composite. A broad peak appears around 25.1° (110) which is attributed to highly doped emeraldine salt,[20] suggesting some degree of crystallinity in PANI. During polymerization, the growth of polymer chain is restricted to some extent in presence of ZrO_2 nanoparticles and the polymer becomes more and more crystalline. The crystallite size of the ZrO_2 nanoparticles in the composite was calculated following the Scherrer's equation[21]

$$D = K\lambda/\beta\cos\theta \quad (1)$$

where $K = 0.89$, D represents crystallite size (nm), λ, the wavelength of CuK_α radiation, and β, the corrected value at half width (FWHM) of the diffraction peak. At $2\theta = 30.3^\circ$ (111 face), which is the characteristics peak of ZrO_2, is chosen to calculate the average diameter and it comes out to be 16 nm, which is consistent with that obtained from transmission electron micrograph (TEM) studies. Tetragonal ZrO_2 can be stabilized at room temperature without doping when the particle size is less than 30 nm.[22,23] The size effect is attributed to the lower surface free energy of the tetragonal form as compared to that of the monoclinic phase. As a result of it, the tetragonal phase becomes more predominant for nanosized particles. In the present investigation, the ZrO_2 nanoparticles having size less than 30 nm are thermodynamically favorable for the stabilization of metastable tetragonal phase.

The TEM micrographs of the nanocomposite sample C1 are shown in Figure 2(a–c). Figure 2(a) is the high resolution transmission electron micrograph (HRTEM) of the bare ZrO_2 nanoparticles, which shows the particles are of spherical shape

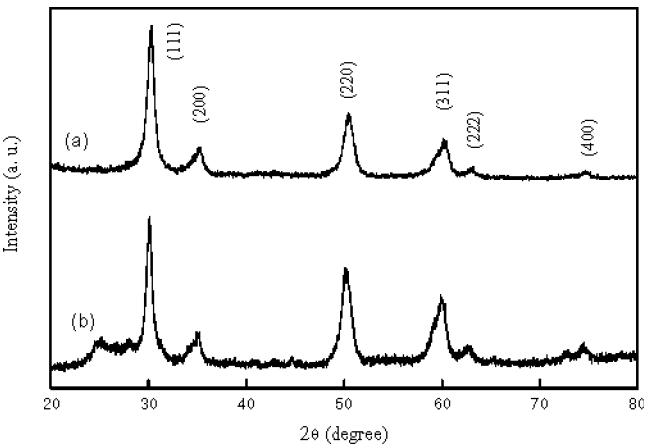

Figure 1 XRD pattern of (a) as synthesized ZrO_2 nanoparticles and (b) ZrO_2-PANI nanocomposite sample C1.

with uniform diameter lying in the range from 15 to 28 nm. Figure 2(b) shows the lower magnification image of the sample C1, which indicates the nanoparticles to be well dispersed in the polymer matrix. The HRTEM of the sample C1 is shown in Figure 2(c). This shows the lattice image from a ZrO_2 nanoparticle in the surrounding of PANI matrix. The lattice spacing is found to be 0.127 nm, which corresponds to (400) plane in t-ZrO_2. So, after the formation of the composites the particles (dark shaded) are found to be encapsulated into PANI (light shaded) chains. This fact is also supported by XRD analysis.

Figure 3(a,b) show the SEM of the pressed powder samples prepared at ambient temperature with highest (C1) and lowest (C5) content of ZrO_2. SEM reveal the grain sizes are of the order of 75–250 nm and it decrease with the increase of ZrO_2 content in the composites. Moreover, the grain becomes more uniform with the increase of ZrO_2 content. The micrographs shown in Figures 2(b) and 3 are different from each other as they were taken in different experimental conditions.

The UV-VIS absorption spectra of the diluted colloidal composite dispersions of two samples (C1 and C3) are shown in Figure 4. The characteristics bands of conducting form of PANI (emeraldine salt) appear at 3.8, 1.8, and 1.3 eV, which are attributed to π-π^*, polaron-π^*, and π-polaron transitions, respectively.[24,25] An additional peak appears at 2.8 eV for all the composites samples indicating PANI in highly doped state. The absence of any peak around 2 eV associated with the quinoid rings eliminates the possibility of formation of insulating form (emeraldine base). The inset shows the same for bare ZrO_2 nanoparticles. A strong absorption starts at around 3.8 eV. The band gap corresponding to the band edge structure gives activation energy of 4.0 eV, which is lower compare to the optical band gap of bulk ZrO_2 as reported ear-

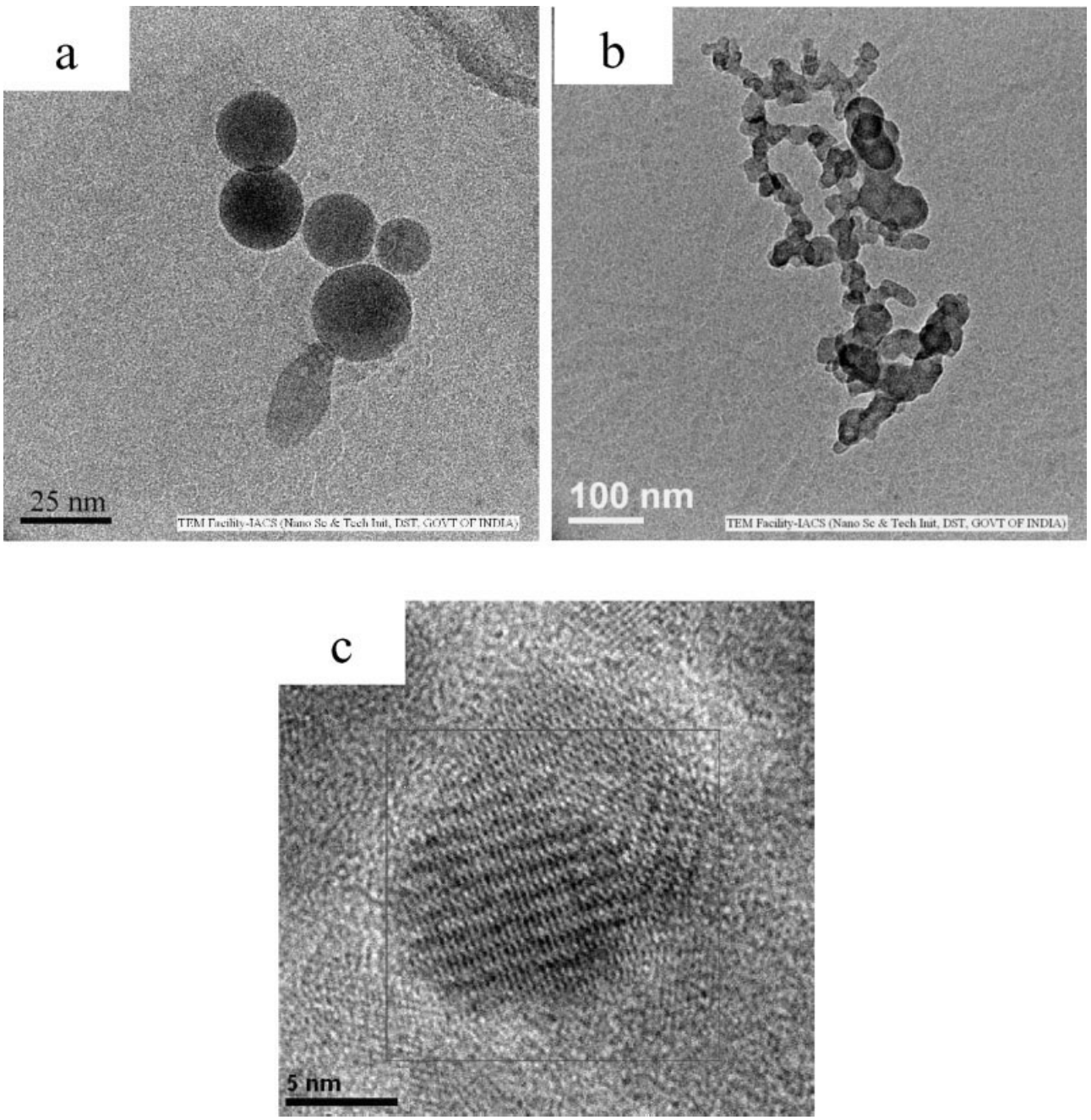

Figure 2 TEM micrograph of (a) bare ZrO_2 nanoparticles, (b) lower magnification image of C1 and high resolution lattice image of C1 in the background of PANI matrix.

lier.[26] This indicates that there is contribution from extrinsic states, such as surface trap or defects states (possible due to Zr^{3+}). The absorption coeffcient α is assessed for the three samples from the equation[27] $\alpha = 2.303 \times 10^3$ Aρ/lc where A is the sample absorbance, ρ is the density of ZrO_2, c is the sample concentration in g/L, and l is the path length.

The optical absorbtion coeffcient (α) near the absorption edge of the semiconductor can be described as[28]

$$\alpha h\nu = A(h\nu - E_g)^m \quad (2)$$

where A is the absorption constant, photon energy is $h\nu$, h is the plank constant and E_g is optical band gap. Generally the optical band gap in a semiconductor is determined by assuming the nature of the transition (m) and plotting $(\alpha h\nu)^{1/m}$ versus $h\nu$, where m represents the nature of the transition. Now m may have different values, such as 1/2, 2, 3/2, or 3 for allowed direct, allowed indirect, forbidden direct, and forbidden indirect transitions, respectively. For allowed direct transition one can plot $(\alpha h\nu)^2$ versus $h\nu$ as presented in Figure 5 and extrapolate the linear

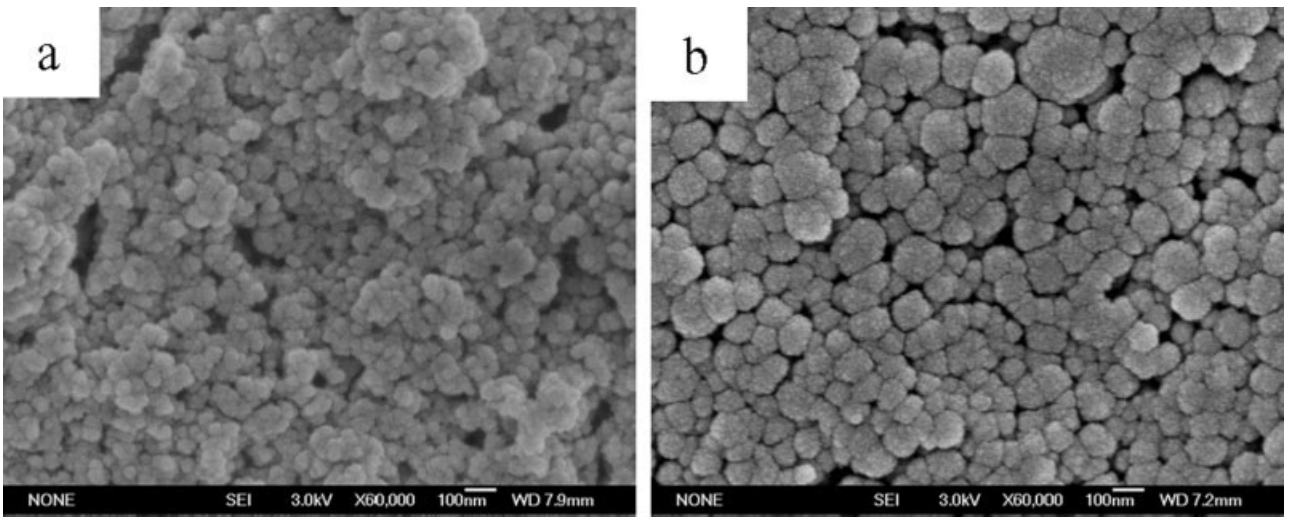

Figure 3 SEM micrograph of the cold pressed powder samples (a) C1 and (b) C5 respectively.

portion of it to $\alpha = 0$ value to obtain the corresponding band gap. In this case $m = 1/2$ and so the interband transition is allowed direct. The estimated band gap for ZrO_2 is 5.12 eV and it decreases from 5.05 eV (C1) to 4.25 eV (C5) with increasing concentration of PANI.

ZrO_2 is a direct band gap insulator with two distinct band to band transitions at 5.2 and 5.79 eV.[29] The highest occupied molecular orbitals (HOMOs) of the valence band are formed by overlapping 2p states of oxygen ions with some admixing of 4 days orbital of Zr^{4+} ions. The lowest unoccupied molecular orbitals (LUMOs) of the conduction band originate from 4 d orbitals of Zr^{4+} ions with some admixing of 2p orbitals of oxygen.[30] The absorption band at 5–6 eV originates due to the transitions from 2p states of oxygen to 4 d states of ZrO_2.

The complex impedance Z^* ($Z^* = Z_1 + iZ_2$) spectra at room temperature for the samples (C1, C2, C4, and C5) as a function of ZrO_2 concentration and pure PANI (C6) are shown in Figure 6. The same spectra for the sample C3 at 303 and 123 K are shown in Figure 7. Figures 6 and 7 indicate that the values of Z_1 and Z_2 decrease with decrease of ZrO_2 concentration. Moreover, two distinct semicircles appear systematically with increase of ZrO_2 content. The temperature variation of impedance spectra for C3 as displayed in Figure 7 exhibits that the diameter of low frequency semicircle is very large compared to that of the high frequency at 303 K. The diameter and the peak value of arc increases with decreasing temperature. Two overlapping semicircles appear in the impedance spectra with lowering of temperature. The impedance spectra consisting of two semicircles are analyzed by an equivalent circuit as shown in Figure 7. Two arcs are represented by two parallel combinations of resistance, R and capacitance, C elements connected in series. One branch is associated with the grain and other with the grain boundary of the samples. The corresponding circuit elements are R_g, C_g and R_{gb}, C_{gb} of grain and grain boundary, respectively. The features of impedance plots are derived from the product RC in the equivalent circuit. The resistance and capacitance of interfacial grain boundary is usually larger than the grain. The high frequency component is the grain contribution and grain boundary effect is associated with the low frequency arc. At low temperature R_{gb} becomes very high which leads to an incomplete arc.

The impedance spectra are deviated from the ideal semicircle whose center lies on the Z_1 axis. The flattened spectra are analyzed by considering the constant phase elements[31,32] (CPE) capacitors $C(\omega) = B(i\omega)^{n-1}$. The parameter B is constant for a given set of experi-

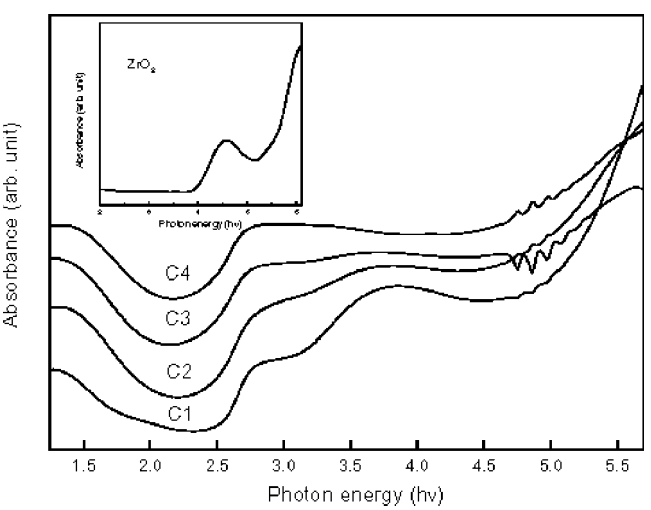

Figure 4 Electronic absorption spectra of the four different nanocomposites (C1–C4) samples. The inset shows the same for pure ZrO_2 nanoparticles.

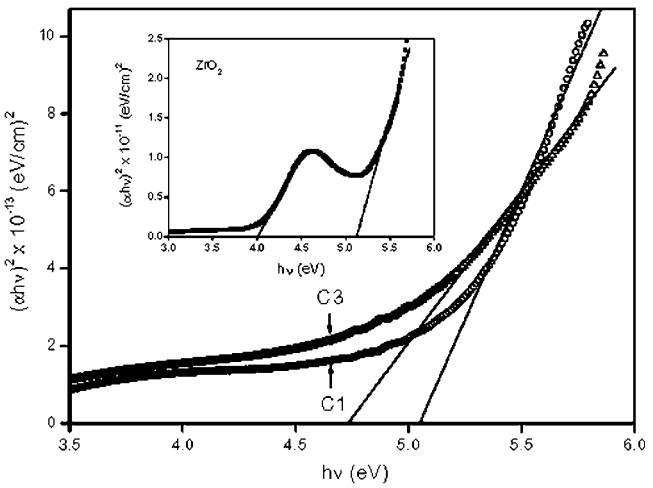

Figure 5 Plot of $(\alpha h\nu)^2$ versus photon energy ($h\nu$) for the two nanocomposites samples (C1–C3) and the inset is for bare ZrO_2 nanoparticles.

mental data. The exponent n varies between 0 and 1. CPE behaves as ideal capacitor for $n = 1$ and ideal resistor for $n = 0$. The experimental data are best fitted employing complex nonlinear curve fitting LEVM program developed by Macdonald.[33] The solid lines in Figure 6 represent the best fitted calculated values.

Grain (σ_g) and grain boundary (σ_{gb}) conductivities are evaluated from the best fitted values of R_g and R_{gb}. The grain conductivity is about two orders of magnitude higher than that of grain boundary as depicted in Table I. Conductivity of ZrO_2 is very low compared to conducting PANI. This gives rise to decrease of σ_g and σ_{gb} with the increase of the concentration of ZrO_2 as shown in Table I.

The temperature dependence of grain and grain boundary conductivity (σ) for all samples are illustrated in Figures 8 and 9, respectively. The straight lines in conductivity σ plot (ln σ vs $1000/T$) indicate thermally activated behavior:

$$\sigma = \sigma_0 \exp(-E/k_B T) \tag{3}$$

Here σ_0 is high temperature limit of conductivity, E is the activation energy, and k_B is Boltzmann constant. The grain boundary (E_{gb}) and grain (E_g) acti-

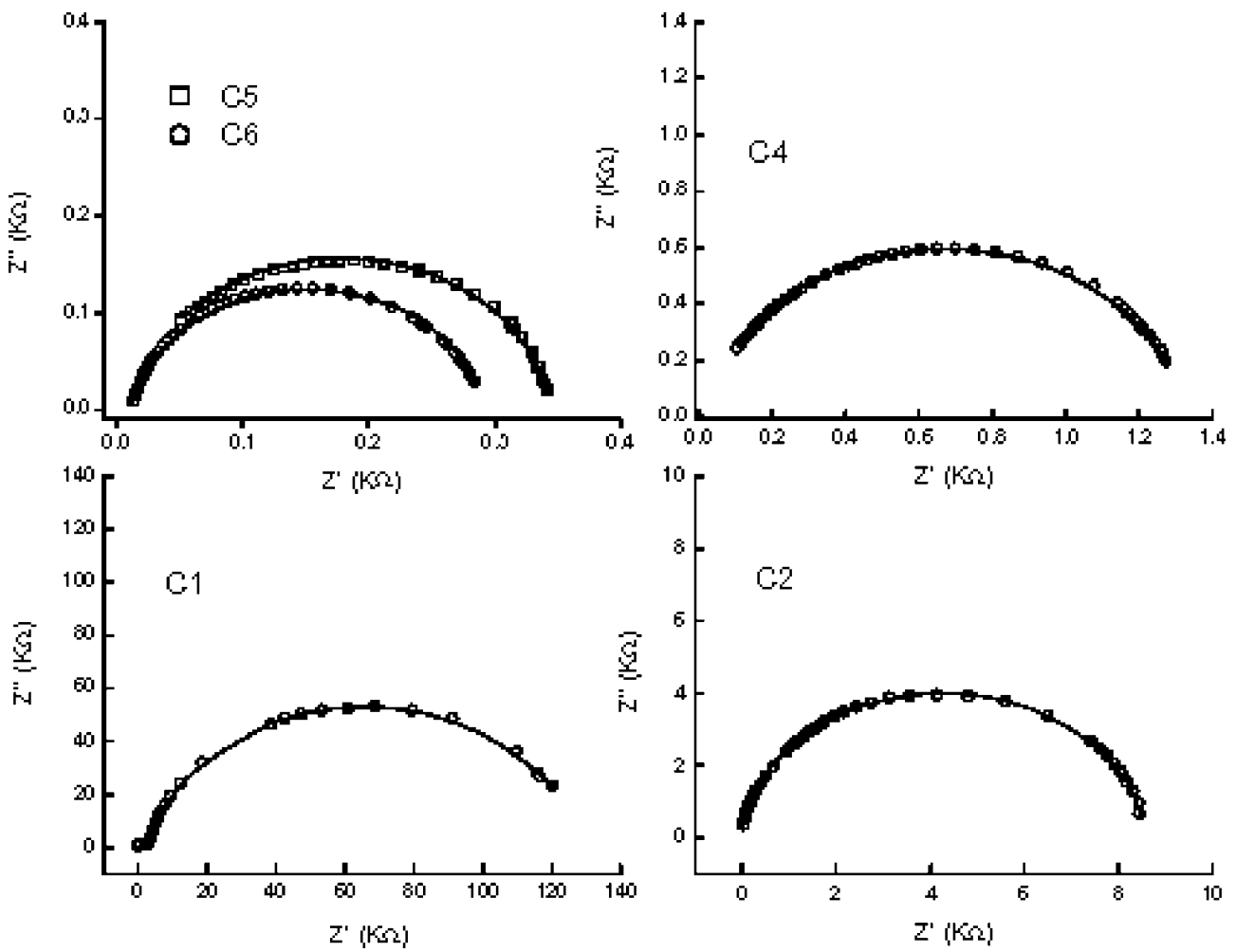

Figure 6 Impedance spectra of the different samples (C1, C2, C4, C5, and C6) at room temperature. The solid lines are fits to the proposed equivalent circuit for the samples.

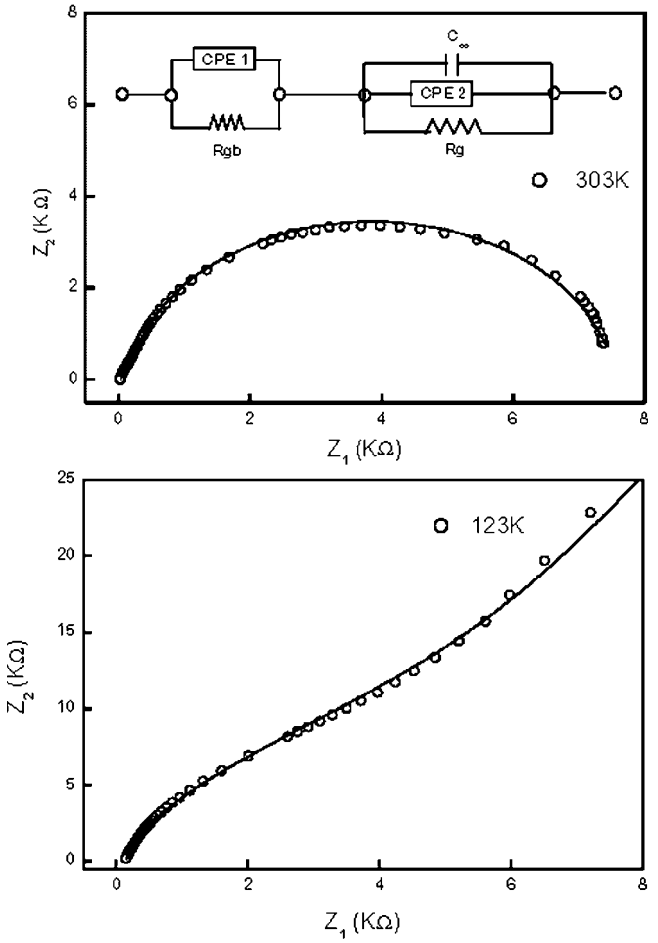

Figure 7 Impedance spectra of the sample C3 at the lowest and highest measured temperatures. The solid lines are fits to the proposed equivalent circuit for the sample.

vation energies are determined from the slopes of straight lines as shown in Figures 8 and 9. The values of E_{gb} and E_g as presented in Table I are quite smaller than usually observed in aliovalent doped ZrO_2 (1 eV).[34] Both E_{gb} and E_g increases with increase of ZrO_2 as shown in Table I except for the sample C3.

Temperature variation of conductivity of PANI is well described by Mott's variable range hopping formalism of amorphous semiconductors.[35]

$$\sigma(T) = \sigma_0 \exp[-(T_0/T)]^\gamma \quad (4)$$

where σ_0 is the high temperature limit of conductivity and T_0 is Mott's characteristic temperature associated with the degree of localization of the electronic wave function. The exponent $\gamma = 1/(1 + d)$ determines the dimensionality of the conducting medium. The possible values of γ are 1/4, 1/3, and 1/2 for three, two, and one-dimensional systems, respectively. One and three-dimensional (3D) charge transport occur in the conducting PANI.[36] In the nanocomposites, Arrhenius type thermally activated conduction is found instead of Mott's variable range hopping within the measured temperature range.

The dielectric constant, ε_1 as a function of frequency at room temperature for different compositions are presented in Figure 10. The inset shows the same for pure PANI. The magnitude and the frequency dependence of ε_1 are strongly dependent on the content of ZrO_2 nanoparticles. In case of more conducting samples, the value of ε_1 is almost independent of frequency. The most important finding is that the nanocomposites exhibit a very high dielectric constant of about 2503 at room temperature for the sample with highest content of ZrO_2. The value of dielectric constant in ZrO_2 varies from 15 to 40 depending on the various crystalline phases.[37,38] Theoretically, it is established that lattice contribution gives a high value of dielectric constant compared to electronic effect. The value of ε_1 for PANI is $\sim$ 400. The present observation of ε_1 is remarkable as it is larger than the constituent materials by six times.

The large dielectric constant of composite systems can be explained by Maxwell–Wagner (MW) type interfacial polarization.[39,40] The dielectric constant of the nanocomposite increases with increase of ZrO_2 content. The encapsulated ZrO_2 nanoparticles play crucial role to enhance the dielectric constant. The electric and dielectric properties of ZrO_2 nanoparticle and PANI are completely different. This leads to a heterogeneous behavior in the nanocomposite. The microstructure consists of grain and gain boundary with different conductivities. The poorly conducting grain boundaries cause an accumulation of charges around the boundary regions. The interfacial MW polarization occurs in the composite containing conducting and more insulating regions. The complex

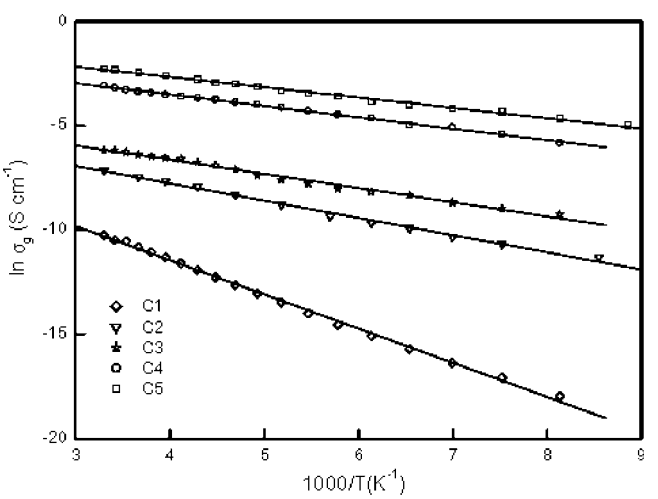

Figure 8 Arrhenius plot of grain conductivity for the five different samples.

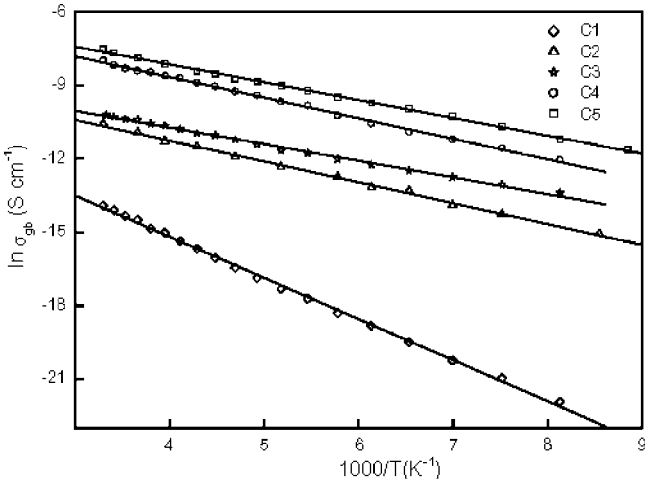

Figure 9 Arrhenius plot of grain boundary conductivity for the different samples.

dielectric constant can be calculated from the relation, $\varepsilon^* = 1/(i\omega C_0 Z^*)$. The static dielectric constant of such system consisting of different conductivities can be expressed as[41]

$$\varepsilon_s = \frac{R_g^2 C_g + R_{gb}^2 C_{gb}}{C_0 (R_g + R_{gb})^2} \tag{5}$$

$C_0 = \varepsilon_0 S/t$ is the geometrical capacitance. For the present materials, $R_{gb} > R_g$ so the static dielectric constant can be approximated from eq. (5),

$$\varepsilon_s = \frac{C_{gb}}{C_0} \tag{6}$$

The estimated dielectric constant from eq. (6) is 5600–1000 which is in good agreement with the experimental result at the lowest frequency. The interfacial polarization arising from different conductivities of grain and grain boundary may be the source for the large dielectric constant.

Different complex formalisms such as impedance (Z^*), dielectric (ε^*), and electric modulus (M^*) are usually used to analyze the main features related to conductivity and permittivity. The peak intensities in Z^* are proportional to the resistance. The large resistance of grain boundary dominates the Z^* spectra over the grain. However, the modulus spectra are very useful to separate grain and grain boundary effects and to study the conductivity relaxation.[42] The electric modulus M^* is defined as

$$M^*(\omega) = M_1 + iM_2 = \frac{1}{\varepsilon^*} = \frac{\varepsilon_1 + i\varepsilon_2}{\varepsilon_1^2 + \varepsilon_2^2} \tag{7}$$

The frequency response of the grain and grain boundary appear in two distinct frequency domains. Grain boundary peaks for C1 and C2 samples fall below the measured frequency interval. Grain peaks are beyond the upper limit of frequency for compositions C4 and C5. Only one peak is found in the entire frequency domain for the nanocomposites (C1, C2, C4, and C5). The real and imaginary components of M^* as a function of frequency are depicted in Figure 11 at various temperatures for sample C3. The grain (peak A) and grain boundary (peak B) peaks are observed in the modulus spectrum for C3. Both the peaks shift to higher frequency with increasing temperature. The magnitude of low frequency peak remains unchanged while that of high frequency decreases with increase of temperature. The peak value depends on the capacitance. The variation of peak value indicates that the capacitance of grain is temperature dependent.

The relatively larger width and asymmetrical nature of peaks suggest the non-Debye process. The shape of M_2 peak has been described by the more generalized Havriliak–Negami (HN) function.[43]

$$M^*(\omega) = M_\infty \left[1 - \frac{1}{(1 + (i\omega\tau)^\alpha)^\beta} \right] \tag{8}$$

where τ is the conductivity relaxation time which is given at the frequency of maximum in M_2 peak. M_∞ is electric modulus at higher frequency. The parameter describes the distribution of the relaxation time of the system. Debye relaxation is obtained for $\alpha = \beta = 1$. The best fitted curves are obtained for $\alpha = 1$; $\beta = 0.54$–0.98 (peak A) and $\alpha = 0.72$–0.99; $\beta = 0.16$–0.98 (peak B) in the entire temperature interval of 123–303 K.

The relaxation times τ at different temperature are determined from the reciprocal of the peak frequency. The Arrehenius plot of ln τ against $1/T$ for the differ-

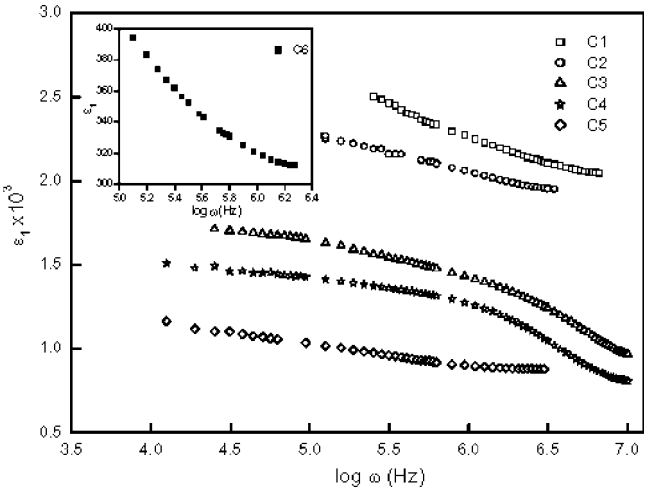

Figure 10 Frequency dependence of the real part of relative dielectric permittivity (ε_1) at room temperature for the five samples. Inset shows the same for the sample C6.

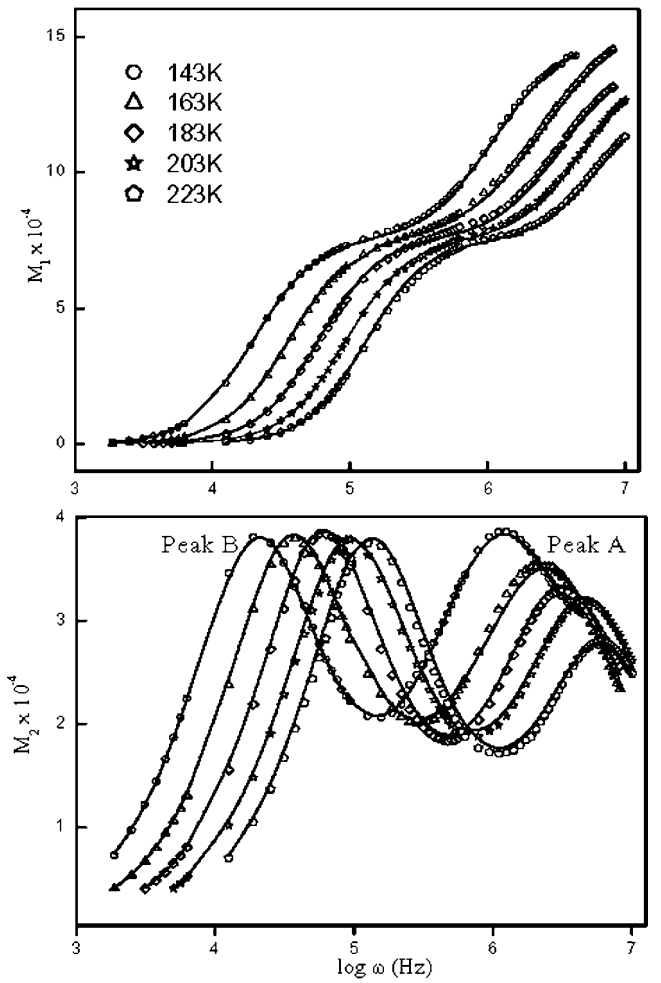

Figure 11 Frequency dependence of real and imaginary component of electric modulus (M_2) at selected temperatures for the sample C3. The solid lines are fits to Eq. (8).

ent samples is shown in Figure 12. A straight line behavior is obtained. Thus, the temperature variation of τ can be described by thermally activated Arrhenius law,

$$\tau = \tau_0 \exp(E_M/k_BT) \quad (9)$$

where τ_0 is the relaxation time at high temperature, E_M is the activation energy of conductivity relaxation process, and k_B is the Boltzmann constant. The slope of the best fitted straight line gives the activation energy as shown in Table I. The temperature dependence of τ follows Arrehenius law similar to conductivity.

Maxwell–Wagner polarization model has been successfully employed to interpret the dielectric and conductivity relaxations in different types of materials.[44–48] Electric modulus is calculated from the relation, $M^* = i\omega C_0 Z^*$ based on the equivalent circuit as shown in Figure 7. The imaginary component, M_2 within the Maxwell–Wagner (MW) formalism can be expressed as[41]

$$M_2 = \frac{C_0}{C_g}\left[\frac{\omega R_g C_g}{1+(\omega R_g C_g)^2}\right] + \frac{C_0}{C_{gb}}\left[\frac{\omega R_{gb} C_{gb}}{1+(\omega R_{gb} C_{gb})^2}\right] \quad (10)$$

The relaxation time for grain and grain boundary responses are $\tau_g = R_g C_g$ and $\tau_{gb} = R_{gb} C_{gb}$. The appearance of peak in M_2 spectra within the measured frequency domain depends on the values of τ_g and τ_{gb}. Two peaks are only observed for the sample C3. The calculated relaxation time for each component is $\tau_g = 8.0 \times 10^{-8}$ s and $\tau_{gb} = 2.4 \times 10^{-6}$ s at room temperature. For all other samples, the deduced values of relaxation times at room temperature are in the range 10^{-6}–10^{-7} s. The overall agreement of the calculated relaxation time with our experimental data suggests that Maxwell–Wagner interfacial polarization appears in the studied materials.

ZrO_2 in stoichiometric composition is a wide band semiconductor and is of very low conductivity. In reality the ratio of Zr : O = 1 : 2 does not occur in most of the cases because of oxygen vacancy. Experimental results confirmed that oxygen vacancy is more prominent upon decreasing of ZrO_2 particle size to nanometer scale.[26,49] The concentration of oxygen vacancy is relatively higher than its bulk counterpart. In the process of oxygen vacancy, free electrons are released in the material, which contribute to electronic conduction. Oxygen vacancy also contributes to ionic conduction at high temperature. Much higher activation energy of ionic conduction rules out this process below room temperature. The electronic conductivity of the nanocomposites is higher than the pure reduced ZrO_2 at 500–1000 K.[50–52] Electrical

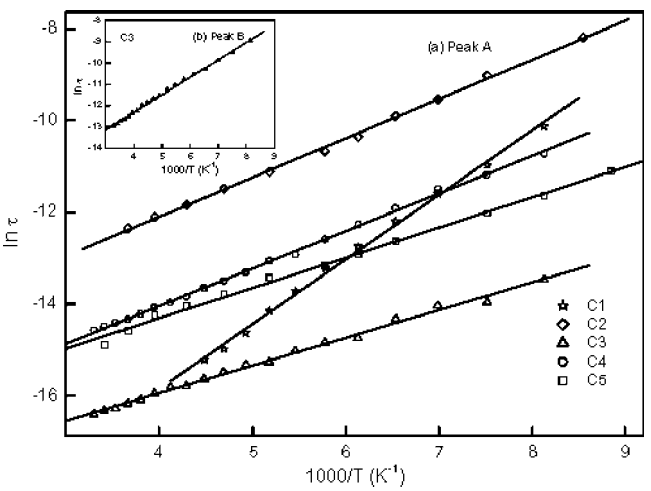

Figure 12 Temperature dependence of relaxation time: (a) of all the samples corresponding to peak A and (b) of C3 corresponding to peak B.

properties of conducting polymer PANI are effected by the preparation condition. ZrO_2 nanoparticles are incorporated within the polymer chain as shown by TEM micrograph. Polymers are formed on the surface of ZrO_2 nanoparticle. Chain lengths are shortened with the increase of ZrO_2 concentration because of enhancement of effective surface area. Hence the conductivity decreases with increase of ZrO_2 content.

Localized energy levels are created in the band gap of ZrO_2 because of oxygen vacancy.[53] Defects states are widened in case of large number of vacancies. The decrease of band gap may due to the formation of energy levels below the conduction band. Zr^{3+} ions are formed for the compensation of charge arising from oxygen vacancy. Different ionic radii of Zr^{3+} and Zr^{4+} ions produce lattice distortion. The oxygen vacancy is mainly concentrated on grain boundary regions. The small peak at lower frequency in M_2 spectra for C3 may originate from the motion of charge carriers between two sites Zr^{3+} at surface and Zr^{4+} in the interior of the nanoparticle. The estimated activation energy is rather small compared to the optical energy gap (4–5 eV of ZrO_2. The large difference between the optical and the thermal activation energies may be due the formation of intermediate impurity levels within the band gap. This forms the mobility edge very close to the conduction band and is responsible for the charge conduction process.

CONCLUSION

Optical energy band gap of ZrO_2 decreases with the increase of PANI concentration. The electrical inhomogeneity induces two conduction processes, which are attributed to grain and grain boundary effects. Larger electronic conductivity and smaller activation energy are due to the formation of localized states arising from Zr^{3+} ions. Higher dielectric constant results from the heterogeneous behavior of semiconducting ZrO_2 and conducting PANI.

Ashis Dey is thankful to Council of Scientific and Industrial Research, Government of India for providing fellowship.

References

1. Claussen, N.; Ruh, M. In Advances in Ceramics; Heur, A. H., Hobbs, L. W., Eds.; The American Ceramic Society: Columbus, Ohio, 1981; p 137.
2. Badwal, S. P. S. Appl Phys A 1990, 50, 449.
3. Miller, T. M.; Grassian, V. H. J Am Chem Soc 1995, 117, 10969.
4. Wilk, G. D.; Wallace, R. M.; Anthony, J. M. J Appl Phys 2001, 89, 5243.
5. Afanasev, V. V.; Houssa, M.; Stesmans, A.; Heyns, M. M. Appl Phys Lett 2001, 78, 3073.
6. Uchikoshi, T.; Sakka, Y.; Ozawa, K.; Hiraga, K. J Mater Res 1998, 13, 840.
7. Garvie, R. C. J Phys Chem 1978, 82, 218.
8. Tuller, H. L. Solid State Ionics 2000, 131, 143.
9. Mondal, P.; Klein, A.; Jaegermann, W.; Hahn, H. Solid State Ionics 1999, 118, 331.
10. Zhang, Y. W.; Jin, S.; Yang, Y.; Li, G. B.; Tian, S. J.; Jia, J. T.; Liao, C. S.; Yan, C. H. Appl Phys Lett 2000, 77, 3409.
11. Guo, X.; Vasco, E.; Mi, S.; Szot, K.; Wachsman, E.; Waser, R. Acta Mater 2005, 53, 5161.
12. Gangopadhyay, R.; De, A. Chem Mater 2000, 12, 608.
13. Gangopadhyay, R; De, A. In Handbook of Organic-Inorganic Hybrid Materials and Nanocomposites; Nalwa, H. S., Ed.; American Scientific Publishers, 2003.
14. Ray, S. S.; Biswas, M. Synth Met 2000, 108, 231.
15. De, A.; Das, A.; Lahiri, S. Synth Met 2004, 144, 303.
16. Bhattachayya, A.; Ganguly, K. M.; De, A.; Sarkar, S. Mater Res Bull 1996, 31, 527.
17. Pang, Y. X.; Bao, X. J Mater Chem 2002, 12, 3699.
18. Gao, L.; Qiao, H. C.; Qiu, H. B.; Yan, D. S. J Eur Ceram Soc 1996, 16, 437.
19. Osseo-Asare, K. In Handbook of Microemulsion Science and Technology; Kumar, P., Mittal, K. L., Eds.; Marcel Dekker: New York, 1999.
20. Pouget, J. P.; Jozefowicz, M. E.; Epstein, A. J.; Tang, X.; Macdiarmid, A. G. Macromolecules 1991, 24, 779.
21. Klug, H. P.; Alexander, L. E. X-ray Diffraction Procedures for Polycrystalline and Amorphous Materials; Wiley: New York, 1954; p 491.
22. Garvie, R. C. J Phys Chem 1965, 69, 1238.
23. Garvie, R. C.; Goss, M. F. J Mater Sci 1986, 21, 1253.
24. Raghunathan, A.; Natarajan, T. S.; Rangarajan, G.; Dhawan, S. K.; Trivedi, D. C. Phys Rev B 1993, 47, 13189.
25. Stafstrom, S.; Bredas, J. L.; Epstein, A. J.; Woo, H. S.; Tanner, D. B.; Huang, W. S.; MacDiarmid, A. G. Phys Rev Lett 1987, 59, 1464.
26. Emeline, A.; Kataeva, G. V.; Litke, A. S.; Rudakova, A. V.; Ryabchuk, V. K.; Serpone, N. Langmuir 1998, 14, 5011.
27. Serpone, N.; Lawless, D.; Khairutdinov, R. J Phys Chem 1995, 99, 16646.
28. Pankove, J. I. Optical Processes in Semiconductors; Prentice Hall: New Jersy, 1971.
29. Kwok, C. K.; Aita, C. R. J Appl Phys 1989, 66, 2756.
30. Morant, C.; Fernandez, A.; Gonzalez-Elipe, A. R.; Soriano, L.; Stampfl, A.; Bradshaw, A. M.; Sanz, J. M. Phys Rev B 1995, 52, 11711.
31. Macdonald, J. R. Impedance Spetroscopy; Wiley: New York, 1987.
32. Jonscher, A. K. Dielectric Relaxation in Solids; Chesla Dielectric Group: UK, 1983.
33. http://www.solartronanalytical.com/downloads/downloads.html
34. Guo, X.; Sigle, W.; Fleig, J.; Maier, J. Solid State Ionics 2002, 555, 154.
35. Mott, N. F.; Davis, E. Electronic Process in Non Crystalline Materials, 2nd ed.; Oxford: Clarendon, 1979.
36. Skothemin, T.; Elsenbaumer, R. Handbook of Conducting Polymers; Marcel Dekker: New York, 1998.
37. Zhao, X.; Vanderbilt, D. Phys Rev B 2002, 65, 075105.
38. Rignanese, G. M.; Detraux, F.; Gonze, X.; Pasquarello, A. Phys Rev B 2001, 64, 134301.
39. Maxwell, J. C. A Treatise on Electricity and Magnetism, Vol. 1.; Oxford University Press: Oxford, 1998.
40. Wagner, K. W. Ann Phys (Leipzig) 1913, 40, 53.
41. Sinclair, D. C.; West, A. R. J Appl Phys 1989, 66, 3850.
42. Macedo, P. B.; Moynihan, C. T.; Bose, R. Phys Chem Glasses 1972, 13, 171.
43. Havriliak, S.; Negami, S. Polymer 1967, 8, 161.

44. Liu, J.; Duan, C.; Mei, W. N.; Smith, R. W.; Hardy, J. R. J Appl Phys 2005, 98, 093703.
45. Ritus, A. I.; Pronin, A. V.; Volkov, A. A.; Lunkenheimr, P.; Loidl, A.; Shcheulin, A. S.; Ryskin, A. I. Phys Rev B 2002, 65, 165209.
46. Papathanassion, A. N. J Phys D Appl Phys 2001, 34, 2825.
47. Bogris, N..; Grammatikakis, J.; Papathanassion, A. N. Phys Rev B 1998, 58, 10319.
48. Huang, C.; Zhang, Q. M.; Su, J. Appl Phys Lett 2003, 82, 3502.
49. Liu, H.; Feng, L.; Zhang, X.; Xue, Q. J Phys Chem 1995, 99, 332.
50. Park, J. H.; Blumenthal, R. N. J Electrochem Soc 1989, 136, 2867.
51. Levy, M.; Fouletier, J.; Kleitz, M. J Electrochem Soc 1988, 135, 1584.
52. Merino, R. I.; Orera, V. M. Solid State Ionics 1995, 76, 97.
53. Foster, A. S.; Sulimov, V. B.; Lopez Gejo, F.; Shluger, A. L.; Nieminen, R. M. Phys Rev B 2001, 64, 224108.